Corrosion Science 230 (2024) 111897

Contents lists available at ScienceDirect

Corrosion Science

journal homepage: www.elsevier.com/locate/corsci

Effect of hydrogen on the microstructure and mechanical properties of $FeCCrNiB_xSi$ advanced high strength steels

Ehsan Norouzi [a], Reza Miresmaeili [a,*], Hamid Reza Shahverdi [a], Mohsen Askari-Paykani [a], Laura Maria Vergani [b]

[a] Department of Materials Engineering, Tarbiat Modares University, Jalal Ale Ahmad Highway, P.O. BOX 14115-143, Tehran, Iran
[b] Department of Mechanical Engineering (DMEC), Politecnico di Milano, Via La Masa 1, 20156 Milano, Italy

ARTICLE INFO

Keywords:
Advanced high strength steel
Hydrogen embrittlement
Dislocation
Boron content
Taylor factor

ABSTRACT

This research provided a thorough knowledge of the hydrogen embrittlement in AHSS models based on $FeCCrNiB_0Si$ (AHSS1) and $FeCCrNiB_2Si$ (AHSS2) alloy systems. The results obtained by electron backscatter diffraction (EBSD) showed the local deformation in the cracked regions. Thermal desorption spectroscopy (TDS) analysis showed despite the higher ratio of irreversible to reversible traps in AHSS2 compared to AHSS1, the susceptibility to HE in AHSS2 was greater than AHSS1 due to the addition of boron and the γ/Cr_2B interfaces' decohesion in the presence of hydrogen. Higher Taylor factor grains in H-charged samples were more likely to suffer plastic instability.

1. Introduction

The usage of Advanced High Strength Steels (AHSS) in the automobile industry has greatly increased passenger safety and lightened the construction of vehicle bodies to satisfy the demands of fuel economy. The AHSS steel grades have usually been developed in recent years to achieve a better balance between strength and ductility. These materials are needed to manufacture the parts of body-in-white constructions that need little forming, such as the central tunnel and crash boxes [1]. The newly formed third generation of AHSS with outstanding ductility and no loss of strength are a more affordable alternative to press hardening steels and Twinning Induced Plasticity (TWIP) Steel. Hydrogen embrittlement (HE) in materials must be taken into account if advancements are to be made in lightweight construction for automobiles. The introduction and diffusion of hydrogen into the metal's crystal structure causes a loss of ductility that ultimately results in brittle fracture [2]. Previous research has shown that the hydrogen impact on material characteristics is enhanced with increasing tensile strength [3]. Because of the high mobility of the hydrogen atom in the crystal structure, hydrogen absorption can occur during the steel-making or automobile-manufacturing processes. Hydrogen-Induced Cracking (HIC) and environmental corrosion are both potential problems that could occur over a vehicle's service life. Therefore, it is important to know how vulnerable steels are to HE, particularly AHSS, in order to ensure the safe use of steels in vehicles. Several research researches [3,4] discuss the influence of hydrogen on the mechanical characteristics of AHSS. Previous studies typically used a variety of testing methodologies to learn more about the mechanism of HIC and the mechanical characteristics of particular steel grades. Even fewer research directly evaluated the different testing methodologies used to assess the HE of AHSS. There is still a lack of experience with how to put research findings into practical applications in industry. As a result of its variability and complexity, hydrogen embrittlement of AHSS remains a significant issue for the automotive industry. In recent years, further theoretical and experimental study on hydrogen embrittlement of AHSS steels have been performed [5–8] Impact toughness and fracture behaviors of AHSSs at low temperatures were studied by Pallaspuro et al. [5]. With the fractographic approach, kernel average misorientation calculations, and cohesive zone modelling, the findings were analyzed in terms of level and active hydrogen embrittlement processes. The results showed that HE occurs at low temperatures, increases the fracture toughness reference temperature, and somewhat decreases the deformation capacity. In another study, Venezuela et al. [6] investigated at how microstructure affected the susceptibility of martensitic AHSSs to hydrogen embrittlement. They found that at high enough hydrogen pressures, transgranular and intergranular fractures initiated near the surface of the sample, where the tensile stress was greatest. They determined that hydrogen-dislocation interactions had a main influence

* Corresponding author.
E-mail address: miresmaeili@modares.ac.ir (R. Miresmaeili).

https://doi.org/10.1016/j.corsci.2024.111897
Received 28 October 2023; Received in revised form 17 January 2024; Accepted 1 February 2024
Available online 5 February 2024

on fracture propagation. The effects of hydrogen on a martensitic AHSS with a tensile strength of 1700 MPa have been evaluated and compared. The hydrogen trace was seen as a decrease in ductility and an increase in shear fracture. There are still many obstacles to overcome when dealing with hydrogen embrittlement in AHSS steels, despite the fact that several numerical and experimental investigations on these phenomena have been conducted in recent years [9,10]. Soluble hydrogen atoms, for example, have a complicated role to play in how they interact with microstructural flaws like grain boundaries, dislocations and also the crystal lattice, all of which may affect mechanical behaviors. Stress-induced increases in hydrogen concentration may also come from hydrogen being trapped during plastic deformation, as noted by Nagumo [11]. Understanding the function of microstructure in hydrogen embrittlement and developing novel steel ideas to prevent hydrogen related deterioration requires the identification of microstructural trap sites and their concentrations in steels [12–14].

Hydrogen embrittlement of AHHS with the novel alloy systems $FeCCrNiB_xSi$ has not yet been understood. The current study is an in-depth investigation of how hydrogen affects the microstructure and mechanical properties of AHSS. The purpose of the research is to clarify the impact of boron concentration on the HE of AHSS in hydrogen charging and H_2 environments. In situ tensile testing and micro indentation at various current densities during hydrogen charging was conducted for the mechanical characteristics. Additionally, the impact of hydrogen on the deformed AHSS's microstructure and the hydrogen induced cracking mechanism were evaluated by EBSD. Finally, analysis of the hydrogen trapping sites of AHSSs was conducted using thermal desorption spectroscopy (TDS).

2. Methods and experimental

The novel AHSSs used in the current research have already prepared by our team in the previous studies [15–18] and details of their production have been reported. The novel AHSSs were prepared using a pressure vacuum caster machine to melt and cast the materials into a water-cooled Cu mold. The master alloy ingot was obtained by Fe-C, Fe-B pre-alloy and commercially pure Fe, Cr, Ni, Si. Two steels with a 1 mm-thick were used for the present study, and the chemical composition in weight percent was shown in Table 1.

The samples were charged electrochemically in aqueous solutions containing 3% NaOH for 20 h at 10, 20, and 30 mA/cm^2 current densities. In-situ tensile testing was carried out just after pre-charging with electrochemical hydrogen at the same current density. A special cell and a powerful jaw were developed for this task. All samples were tested using Instron equipment at a tensile speed of 0.1 mm/min and a maximum applied load of 20 tons. All test conditions were conducted three times with the average of results reported. The microstructures after deformation were studied by stopping the tensile tests at different strains. Tensile tests were interrupted at a strain of 83% for AHSS1 and a strain of 6% for AHSS2.

After pre-charging, both the uncharged and charged samples were put through micro-indentation testing. Indentations with depths ranging from 20 to 100 micrometers and spacing of 20 micrometers were implemented utilizing a constant displacement model. During indentation testing, the loading and unloading speeds were both 5 μm/s. The findings of each indentation test were given as the average of three distinct measurements. The penetration test results in a graph showing load (F) vs penetration depth (h_p). The plastic deformation energy, often known as the indentation energy (G_{IE}), is the definite integral of P-h_p. When the indentation energy at h_p attains a critical value (G_{IEF}), a hypothetical fracture occurs, which is shown as [19–28]:

$$G_{IEF} = \int_0^{h_p^*} F(h_P)\Big) dh_p = \int_0^{h_0^*} \frac{F(h_p)}{A_p(h_p)} dh_p \quad (1)$$

P represents the indentation pressure, F represents the indentation load, and A_p denotes the plastic area in the provided equation.

$$A_P = 23.75 h_p^2 \quad (2)$$

The following equation can be used to establish a relationship between G_{IEF} and strain energy density:

$$G_{IEF} = \frac{S_{cr}(1-\vartheta)}{(1-2\vartheta)} \quad (3)$$

In Eq. 3, The symbol S_{cr} denotes the strain energy density, while the symbol ϑ represents the Poisson's ratio of the material, which was supposed to be 0.30 in the prior equation. S can be considered as the extension energy of a fracture when it reaches its critical value (S_{cr}). S_{cr} denotes fracture toughness, and the following equation illustrates its relationship to K_{IC} [19–28].

$$K_{IC} = \sqrt{\frac{2ES_{cr}}{(1+\vartheta)(1-2\vartheta)}} \quad (4)$$

Fracture toughness must be computed using the critical indentation depth (h_p). Consequently, the effective material elastic modulus (E) and the reduced material elastic modulus (E_r) must be calculated using the calculations provided below [19–28]:

$$A_c = 24.504 h_c^2 \quad (5)$$

$$E_r = \frac{k.\sqrt{\pi}}{2\beta.\sqrt{A_c}} \quad (6)$$

$$\widetilde{E} = \frac{(1-\vartheta^2)}{\left(\frac{1}{E_r} - \frac{1-\vartheta_i^2}{E_i}\right)} \quad (7)$$

The symbols have the corresponding meaning in the equations above; h_c refers to the elastic contact depth, E represents the modulus of elasticity of the indenter tip, equal to 900 GPa, ϑ_i is the Poisson's ratio of the indenter, equal to 0.02, A_c denotes the contact area, K signifies the unloading stiffness for the Vickers indenter, β refers to a correction factor for axial symmetry loss, set at 1.0124. Once E was calculated for different values of h_c, the relationship between hp and E could be inferred. The ln h_p -ln $\widetilde{E}$ curve shows a linear trend that can be expressed by a simple equation [19–28].

$$\widetilde{E}_{min} = 0.51E \quad (8)$$

Using the material's elastic modulus (E 210 GPa), the above equation can be used to compute the module of effective elastic at the imagined fracture starting point ($\widetilde{E}_{min}$). When Eq. 8 is used to get E_{min}, the linear equation between ln h_p and ln $\widetilde{E}$ may be utilized to calculate h_p. Now, G_{IEF} can be computed by substituting h_p in Eq. 1, and S_{cr} can be calculated using Eq. 3. Finally, the fracture toughness will be calculated using Eq. 4 [19–28].

SEM and electron backscattered diffraction (EBSD) were used to investigate the microstructures of the as-received microstructures as well as deformation microstructures with and without hydrogen

Table 1
The chemical composition of steels (wt%).

Steel designation	C	Si	Mn	P	S	Cr	Mo	Ni	Co	N	B	Fe	other
AHSS1	0.45	3	-	-	-	15.5	-	14.1	-	-	-	base	< 0. 2
AHSS2	0.45	3	-	-	-	15.5	-	14.1	-	-	2	base	< 0. 2

charging. Using carbide sheets and diamond polishing (3 and 1 μm), Interrupted tensile testing specimen cross-sections were polished. Vibrato polishing and electrochemical polishing with 6% perchloric acid and 94% acetic acid were used to prepare specimens for EBSD measurements. For the examination of EBSD data, the HKL-Channel 5 system was implemented.

TDS was conducted on H-charged materials to measure the hydrogen concentration and desorption behavior. The studies were conducted using a Bruker analyzer equipped with a mass spectroscopy detector and a heating rate of 20 °C/min. The hydrogen concentration was determined by measuring the amount of hydrogen desorbed from room temperature to 600 °C.

3. Results

3.1. Initial microstructure

Fig. 1 presents the microstructure of AHSS1 and AHSS2 characterized by EBSD. The EBSD inverse pole figure (IPF) maps (Fig. 1b, f) indicate that two steels are fully recrystallization and display random grain orientation with average grain size of 24 μm and 2 μm for AHSS1 and AHSS2, respectively. According to EBSD phase maps, the AHSS1 has a microstructure consisting of FCC-γ phase and $Cr_{23}C_6$ (Fig. 1c). on the other hand, AHSS2 composed of FCC-γ, Cr_2B, and α-Fe phase as shown in Fig. 1g. The average dimensions of Cr_2B and $Cr_{23}C_6$ phase were 2.1 μm and 0.9 μm, respectively. The EDS maps of chrome and boron are presented in Fig. 1d, h. Table 2 shows the basic indexing of different phases in the microstructure.

3.2. Tensile Test

Fig. 2. shows the stress-strain curves of H-free and H-charged samples from in situ tensile test. Compared with specimen 0B, boron addition resulted in an increase in both the YS and UTS due to greater solid solution strengthening. Clear different in mechanical properties can be seen between uncharged and hydrogen charged samples. For AHSS1, the UTS decreased from 610 MPa to 586 and 568 MPa after hydrogen charging of 10 and 30 mA/cm^2, respectively. For AHSS2 the ultimate tensile strength decreased from 1169 MPa to 1111 and 1011 MPa after hydrogen charging. In situ hydrogen charging had significant effect on elongation to fracture. After H-charging at 30 mA/cm^2, elongation changed from 97% to 83% for AHSS1, and from 8.7% to 5.9% for AHSS2. The hydrogen embrittlement index (I_{HE}) used to evaluate the hydrogen induced elongation loss is described as Eq. 9 [29], where $E_{uncharged}$ and $E_{charged}$ represent strain to failure of uncharged and charged specimens, respectively.

Table 2
The basic indexing and crystallographic information of phases in AHSSs.

Phase	Crystal structure	Space group	Lattice parameters (Å)
γ-FCC	Cubic	Fm-3 m	a=b=c= 3.6599
α-BCC	Cubic	Im-3 m	a=b=c= 2.866
$Cr_{23}C_6$	Cubic	Fm-3 m	a=b=c= 10.6595
Cr_2B	Tetragonal	I4/mmc	a=b= 5.185, c= 4.316

$$I_{HE} = \frac{E_{Uncharged} - E_{Charged}}{E_{UnCharged}} \times 100 \quad (9)$$

Significant losses were detected in total elongation with hydrogen charging, as shown in Table 3; the losses were 14% and 32% for AHSS1 and AHSS2, respectively. This means that AHSS2 is more prone to hydrogen embrittlement than AHSS1. The mechanical properties of the stress-strain curves are summarized in Table 3.

3.3. Indentation Test to Determine Fracture Toughness

Load-displacement plots for both charged and uncharged indentation test samples are shown in Fig. 3. Hydrogen pre-charging decreased the maximum indentation forces for each displacement.

Graphs of the Ln (E)-Ln h are shown in Fig. 4a, c. Critical value of E = 109.2 GPa was extrapolated to its corresponding depth (hp*) for this calculation. Fig. 4b, d presents the F-hp curves for both uncharged and charged specimens. Once the force equation and h_p * are known, the fracture toughness (K_{IC}) and the fracture energy (G) were calculated. Fig. 5 displays the K_{IC} and G value difference between reference and charged samples. The fracture toughness calculated decreased from 245 to 232 MPa.m$^{0.5}$ for AHSS1 and from 225 to 208 MPa.m$^{0.5}$ for AHSS2.

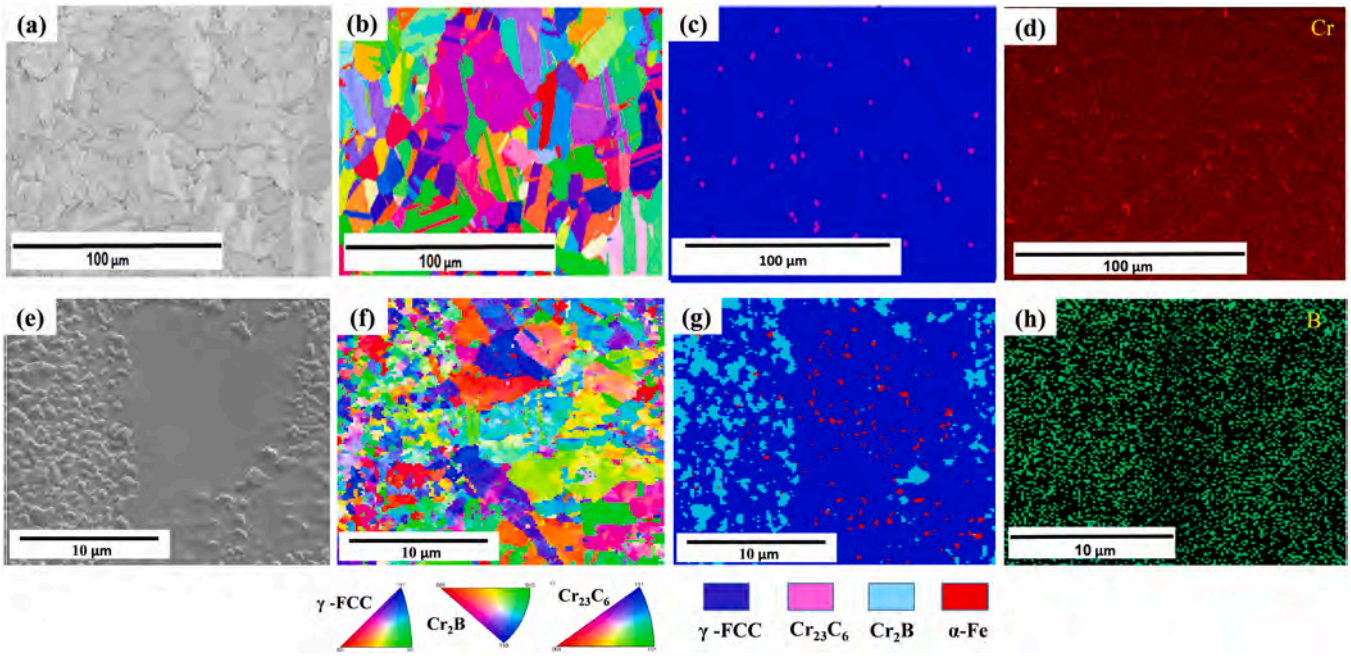

Fig. 1. Microstructure of AHSS1 and AHSS2. a, e) SEM, b, f) IPFs, c, g) Phase maps, d, h) EDS map.

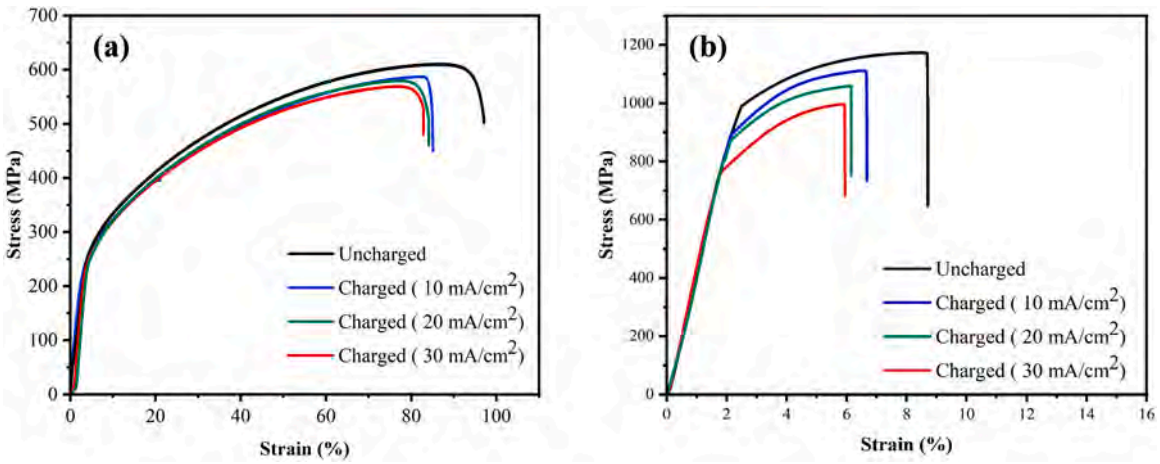

Fig. 2. Engineering stress-strain curves with and without hydrogen charging, a) AHSS1, b) AHSS2.

Table 3
Stress-strain curves results for all samples in air and H-charged at 10, 20, and 30 mA/cm^2.

Specimen designation	Environment	Current density (mA/Cm^2)	YS (MPa)	UTS (MPa)	Elongation (EI %)	Hydrogen embrittlement Index (I_{HE})
S1	Air	n/a	272 ± 7	610 ± 8	97 ± 2	n/a
S1	NaOH	10	270 ± 5	586 ± 2	85 ± 1	12
S1	NaOH	20	270 ± 3	574 ± 6	84 ± 2	13.5
S1	NaOH	30	269 ± 6	568 ± 6	83 ± 3	14
S2	Air	n/a	993 ± 8	1169 ± 9	8.7 ± 1	n/a
S2	NaOH	10	889 ± 7	1111 ± 14	6.5 ± 0.3	25
S2	NaOH	20	897 ± 4	1059 ± 8	6.2 ± 0.1	28
S2	NaOH	30	759 ± 4	1011 ± 11	5.9 ± 0.2	32

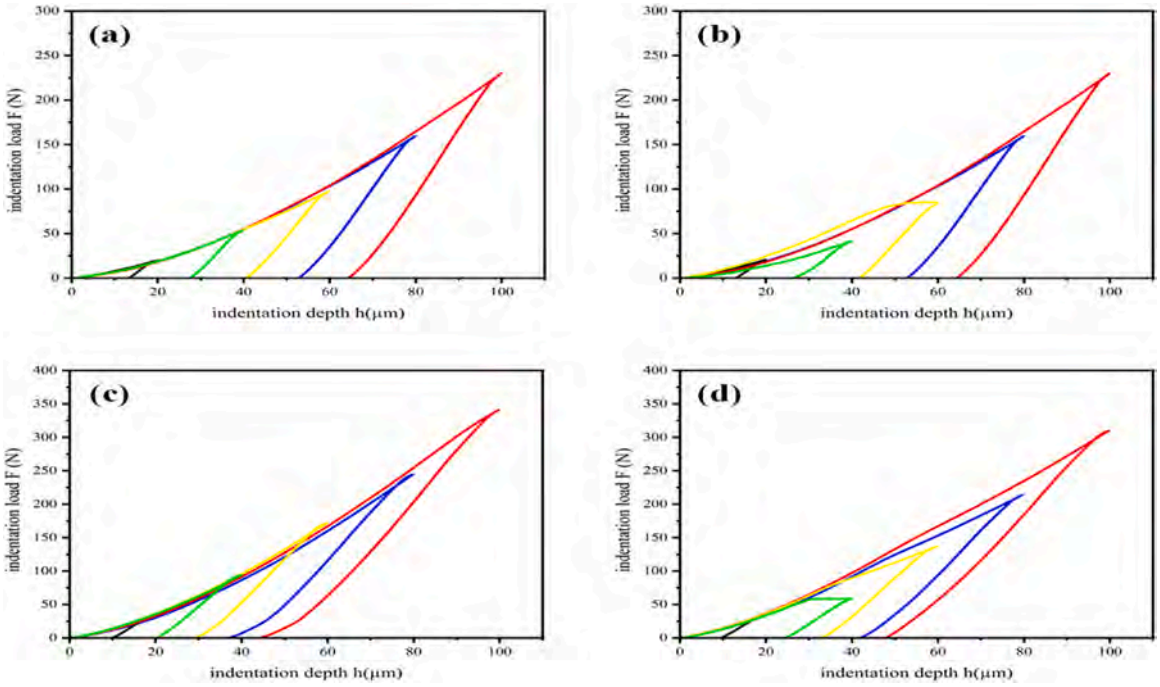

Fig. 3. Diagrams illustrating the load-displacement of specimens: a, c) uncharged, b, d) charged.

3.4. Microstructure evaluation

EBSD was performed in order to reveal the effect of hydrogen on the deformation microstructures. Figs. 6, 7 illustrate IPFs and Kernel average misorientation (KAM) of interrupted tensile test samples for both uncharged and charged condition. KAM maps can be used to determine the dislocation density of the samples. The KAM values were computed using the EBSD points of the first neighbor. As a result, the local plastic strain was qualitatively evaluated, where a high value denotes a considerable degree of deformation or a high density of defect

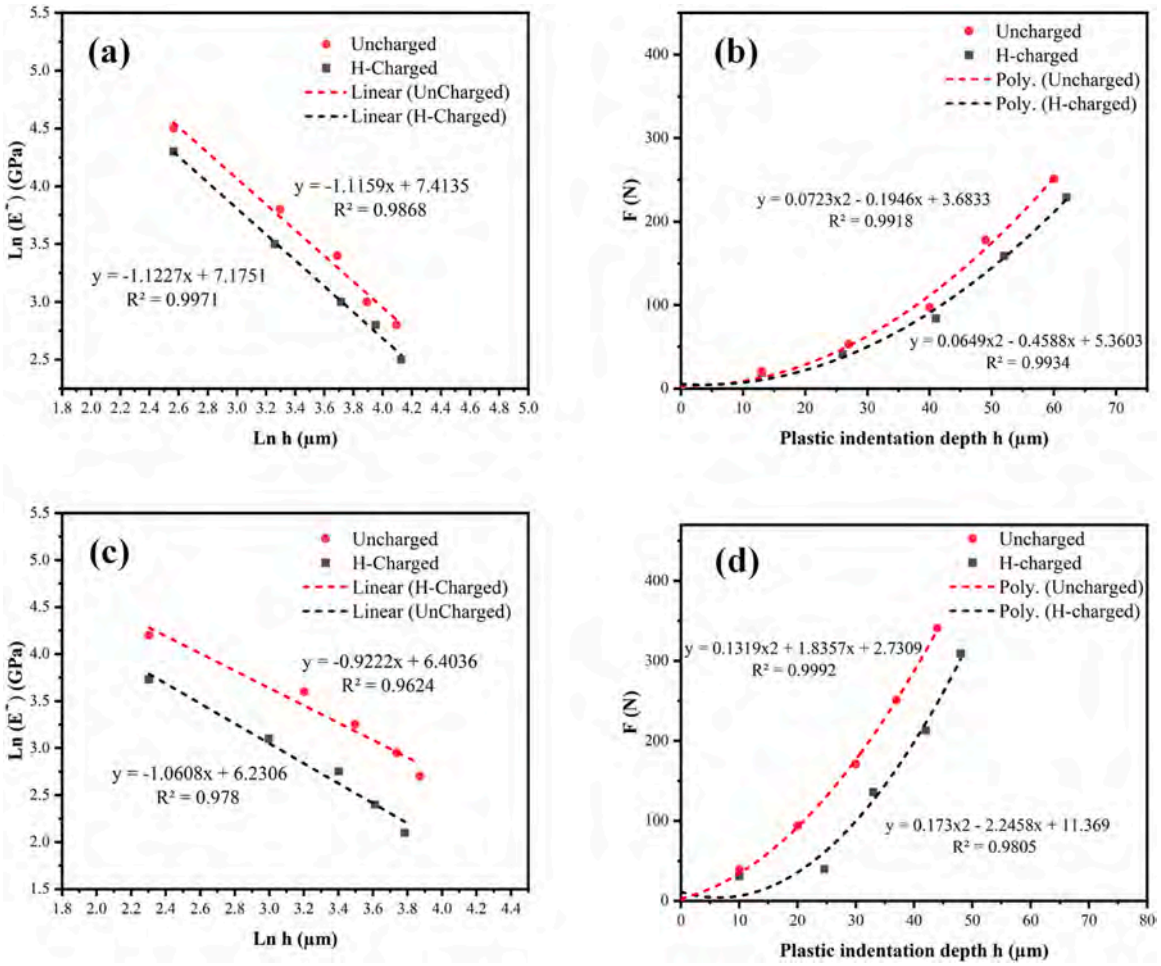

Fig. 4. Ln (E~)-Ln (h) curves of specimens a) AHSS1, c) AHSS2, and F-h diagrams of samples b) AHSS1, d) AHSS2.

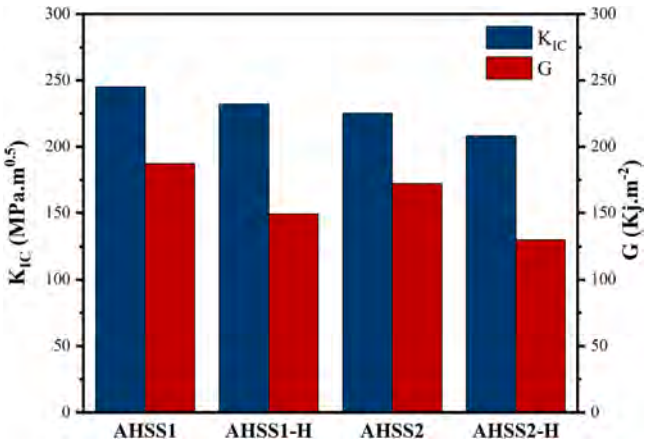

Fig. 5. Comparison of fracture energy and fracture toughness for uncharged and H-charged specimens.

[30]. Eq. 10 [31,32] can be used to compute the average KAM:

$$KAM\left(po\ \mathrm{int}\ j\right) = \frac{1}{N}\sum_{K=1}^{N}\omega(g_i, g_j) \qquad (10)$$

where N is the total number of nearby EBSD points that meet the threshold misorientation value, often 5°, and (g_i, g_j) is the misorientation angle, or the difference between the orientations of the neighboring point (g_i) and point j itself (g_j). Software developed by Channel 5 was utilized to process the EBSD findings that were used in Eq. 10. The average KAM distribution of the uncharged and charged samples in AHSS1 was 1.9° and 2.65° on the other hand, the average KAM value for uncharged and charged samples was 0.65° and 0.95° for AHSS2. The KAM_{avg} of H-specimens are higher than those H-free samples according to the KAM distribution maps. It can be deduced that the dislocation density increased after hydrogen charging at the same level of deformation.

The EBSD maps of crack nucleation of hydrogen charged sample for AHSS1 after tensile test is shown in Fig. 8. Fig. 8c portrays that The KAM around the crack is high, while the other regions exhibit homogenous KAM distribution, revealing the greater local deformation near the crack compared to far field areas. In addition, it can be seen that cracks are initiated from $Cr_{23}C_6$ phase.

Fig. 9. presents the crack morphology of AHSS2 after hydrogen charging by EBSD. It can be seen that the crack growth propagated through γ/Cr_2B interface as shown in Fig. 9b. In addition, the sample has much greater KAM value near the crack, causing strain localization.

3.5. TDS analysis

Fig. 10 shows the TDS curves of the AHSS1 and AHSS2 at a heating rate of 20 °C/min for both current densities of 10 and 30 mA/cm^2. Both steels exhibited three distinct peaks. The initial peaks of both steels show in the 100–200 °C range, indicating reversibly trapped hydrogen with hydrogen contents of 4.26 and 4.98 wppm, respectively. Meanwhile, the second peaks of two steels appear at temperatures between 350 and

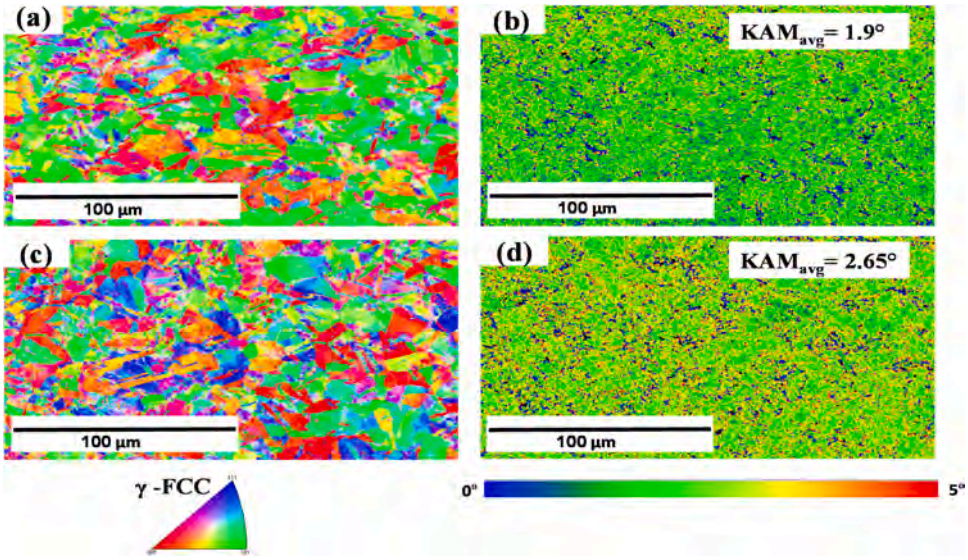

Fig. 6. IPF maps and KAM maps obtained from EBSD analysis on interrupted tensile test at strain of 83% for AHSS1 (a, b): uncharged, (c, d): H-charged.

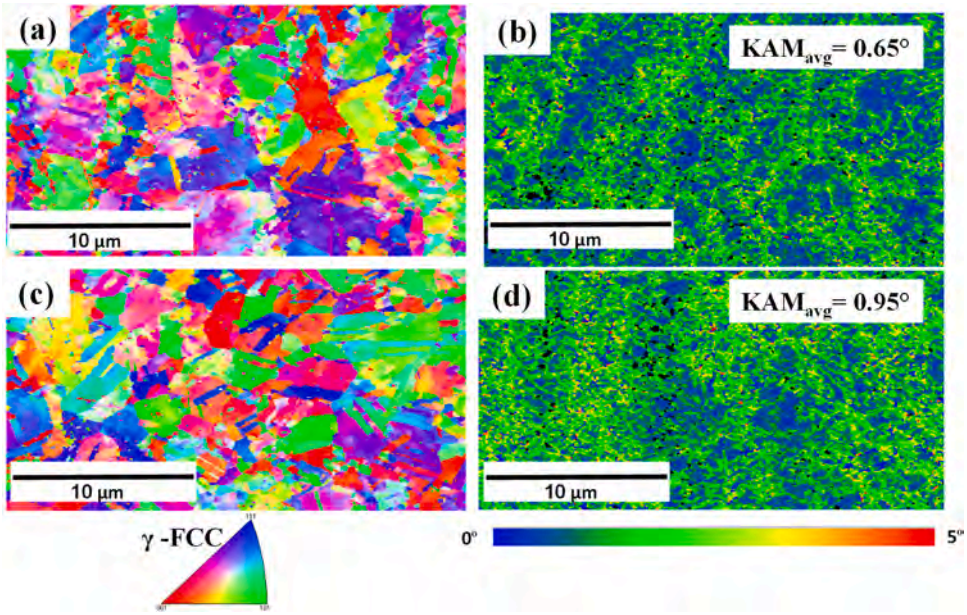

Fig. 7. IPF maps and KAM maps obtained from EBSD analysis on interrupted tensile test at strain of 6% for AHSS2 (a, b): uncharged, (c, d): H-charged.

400 °C, corresponding to 0.21 and 0.13 wppm of irreversibly trapped hydrogen after hydrogen charging of 30 mA/cm^2, respectively. The graphs show the second peak in AHSS2 with lower hydrogen intensity than the second one in AHSS1. Furthermore, the third peak found in both samples at 500 °C shows an irreversible hydrogen trapping site. The hydrogen concentrations of third peak in AHSS1 and AHSS2 were 0.17 and 1.2 wppm, respectively. It is obvious that the intensity of the third peak in AHSS2 is greater than that of the third one in AHSS1.

4. Discussion

In this study, in order to acquire understanding of the mechanisms of hydrogen embrittlement and the effect of boron on mechanical characteristics in the presence of hydrogen, AHSS1 (B=0%wt) and AHSS2 (B=2%wt) have been subjected to pre-charging and in-situ hydrogen charging. The ductility of tensile samples and the fracture toughness of both steels were significantly affected by hydrogen charging, Figs. 2, 5. The level of property deterioration was a substantial function of composition. The hydrogen embrittlement of steels could be caused by a variety of processes, including as the creation of hydride, adsorption induced dislocation emission (AIDE), the hydrogen enhanced decohesion mechanism (HEDE), and the hydrogen enhanced local plasticity model (HELP) [33,34]. This points to the importance of H in the material's microstructural development. The indentation test results demonstrated a 5% and 7.5% decrease in fracture toughness after hydrogen charging for AHSS1 and AHSS2, respectively (Figs. 3, 4 and 5). Hydrogen diminishes the material's atomic bonding, decreasing its ductility and encouraging brittle fracture behavior. This can reduce the material's fracture resilience, making it more susceptible to sudden and calamitous failure. It was reported [35] that fracture toughness was measured using the indentation method following hydrogen pre-charging of samples, and the results were in good agreement with those measured using other common methods. Numerous studies [36, 37] additionally determined fracture toughness through the indentation

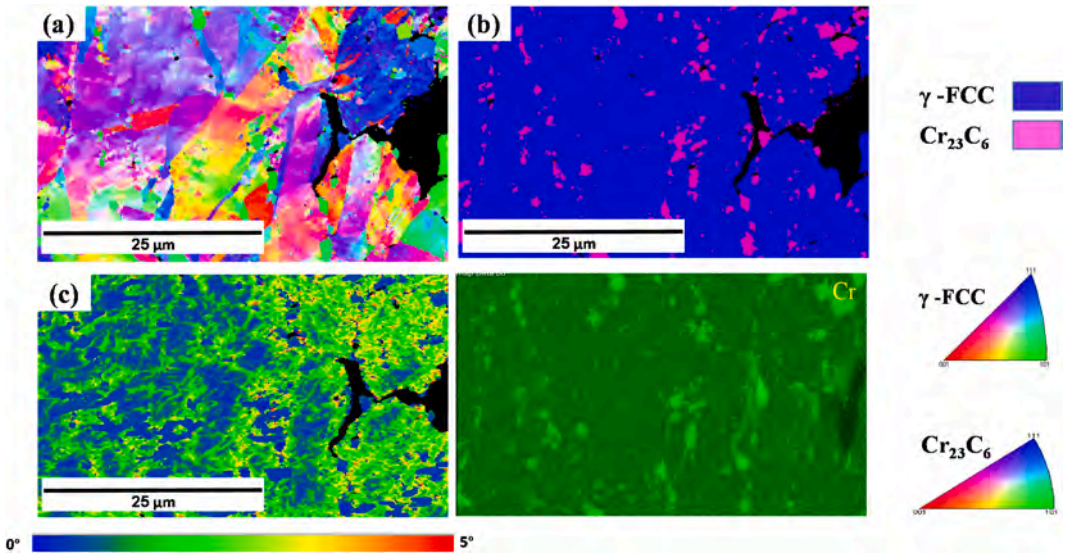

Fig. 8. EBSD IPF map, phase map, KAM, and EDS map of cracked area of AHSS1 in the H_2 environment.

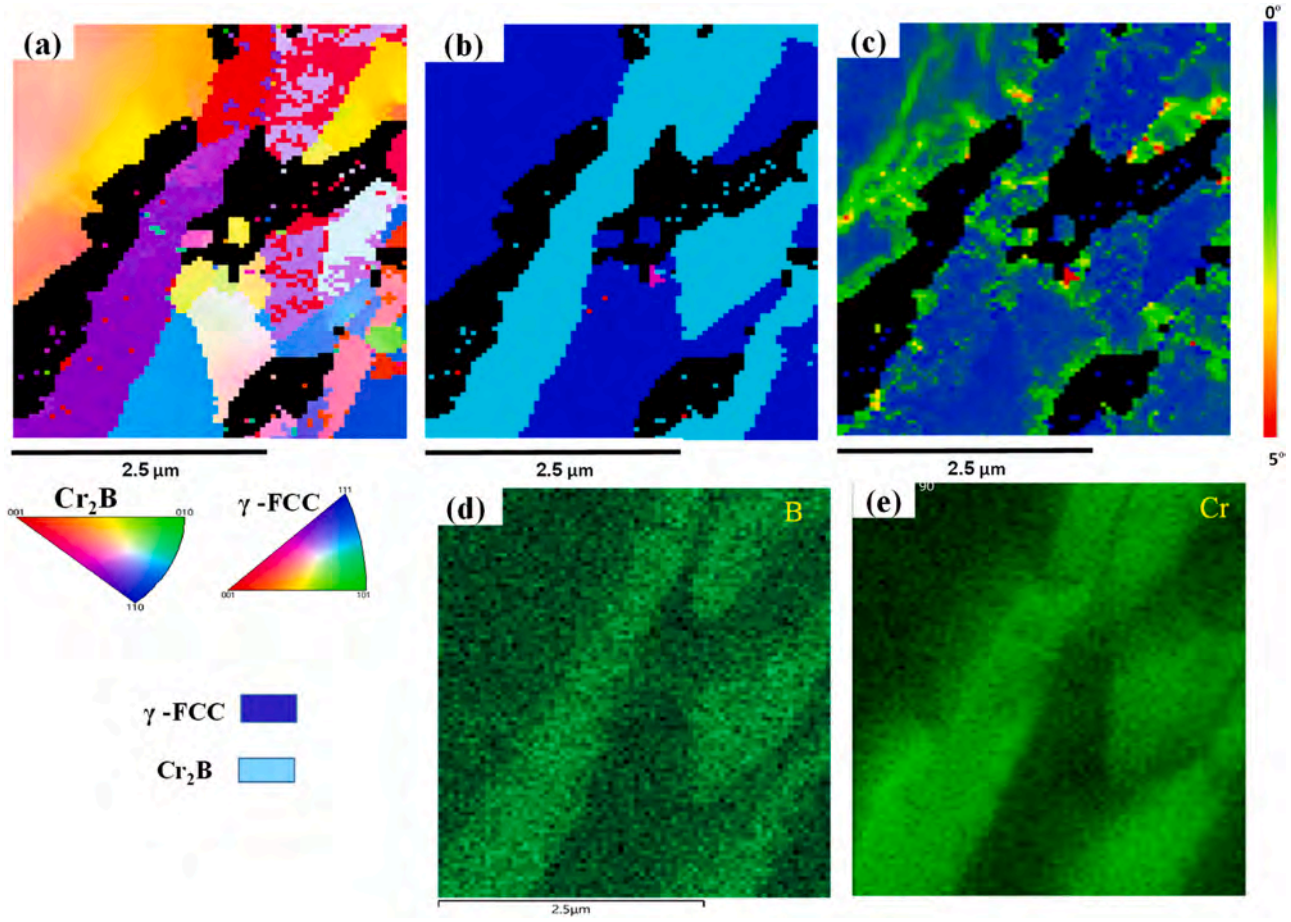

Fig. 9. EBSD IPF map, phase map, KAM, and EDS maps of cracked area of AHSS2 in the H_2 environment.

technique and reported a high degree of concordance between the results obtained using this method and those obtained using other prevalent techniques.

By shielding the elastic stress field created by dislocations, hydrogen surrounding dislocations lowers their contact with impediments, enabling dislocations to move under lower stress and facilitating dislocation migration [38–40], as described by the hydrogen-enhanced localized plasticity (HELP) mechanism. Therefore, during plastic deformation, Hydrogen atoms inside grains would rapidly and continually migrate with dislocations to high-stress concentration areas like fracture tips and grain boundaries, leading to a massive buildup of hydrogen atoms at these regions, Figs. 6, 7. The hydrogen-enhanced

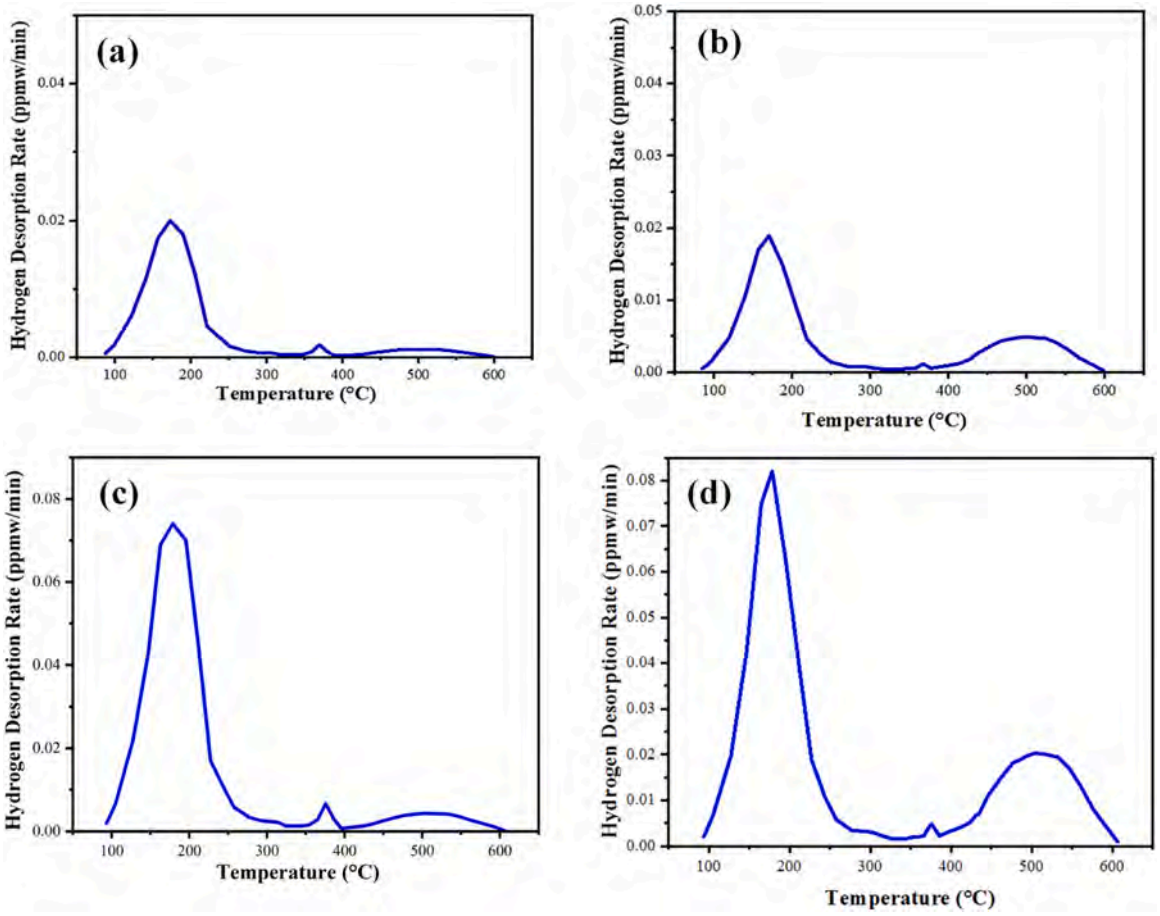

Fig. 10. Hydrogen desorption curves of a) AHSS1, b) AHSS2 pre-charged at 10 mA/cm^2, and c) AHSS1, d) AHSS2 pre-charged at 30 mA/cm^2.

decohesion (HEDE) mechanism implies that hydrogen atoms weaken atomic bonds, which in turn increases the possibility of cracking under high stress concentrations caused by external forces, Figs. 8, 9. The HEDE mechanism was raised to interpret the load relaxation and intergranular failure caused by hydrogen. As shown in the Figs. 8, 9. intergranular cracks in the presence of hydrogen are observed in two steels. Similar findings have been reported in the literature [41,42]. These findings suggest that both HELP and HEDE mechanisms are the causes of the delayed fracture of two steels. Motion dislocations move hydrogen atoms inside grains, where they eventually aggregate on grain borders and contribute to the localized stress concentrations that develop at these locations. According to Martin et al. [43], hydrogen is thought to accelerate the interaction and development of dislocations, so that if hydrogen concentrations are high enough at grain boundaries, the work hardening associated with hydrogen-enhanced plastic processes would result in an increase in local deformation, which will cause intergranular cracking when grain boundaries reach the fracture strength, as can be seen in Figs. 8, 9. In a detailed analysis of the hydrogen-induced quasi-cleavage facet in 22MnB$_5$ steel, Cho et al. [44] showed that dislocation movement causes the quasi-cleavage fracture mode. Increasing dislocation density efficiently strengthens the matrix and produces high local stress, allowing hydrogen to accumulate at the preceding austenite grain boundaries and lowering the cohesive energy of the boundaries, Figs. 6, 7.

The findings under hydrogen charging revealed that the B content addition to AHSS increased the susceptibility to HE. The HE properties of steel would be clearly dependent on the microstructure, such as volume fraction and morphology. The only difference between AHSS1 and AHSS2 is the boron content. In other words, the boride phase is present in the morphology of AHSS2 as compared to AHSS1 as shown in Fig. 1. It was reported that the second hard phase dispersed in the soft matrix phase might influence fracture formation [45]. The plate-shaped M_2B phases stay elastic, whereas the soft grains yield during deformation and near the crack tip. Internal stresses are increased at the γ/plate-shaped M_2B interfaces due to plastic strain incompatibility [15]. As a consequence, the interfaces decohere, and the crack growth route follows the γ/plate-shaped M_2B interfaces, as illustrated in Fig. 9. In other words, it was reported that the addition of boron led to the strain incompatibility between the austenite grains and boride phases [15,18]. However, hydrogen could enhance the localization of deformation and incompatibility at the austenite/M_2B interface due to higher dislocation density as shown in Fig. 9. This could be implied by HELP mechanism, accelerating the nucleation of micro-voids. The plastic instability caused by the occurrence of boride precipitates in the hydrogen-charged specimen, leading to crack propagation. Consequently, it can be interpreted that the greater susceptibility of AHSS2 to HE than in AHSS1 could be attributed to boride precipitates (Cr_2B phase) at the grain boundaries.

TDS provides information about trapping and is a mix of numerous elements, making interpretation difficult, Fig. 10. Moreover, for precipitates, even minor changes in composition or the nature of their interaction with the matrix can have a significant impact on their ability to trap hydrogen. The first, second, and third peaks for two steels are recognized to represent dislocations, austenite phase, and precipitates, respectively, based on the experimental work given in this paper and previous research [46]. There is a difference between the two steels in the dislocation density and volume percentage of austenite. It seems that AHSS1 had more dislocation than AHSS2, resulting in increased trapping at these locations and hence a bigger TDS peak. On the other hand, AHSS1 had a larger proportion of austenite than AHSS2, indicating that more hydrogen was trapped in the second peak. Another significant

finding from the current research based on the combined microstructure and TDS analysis is that the addition of boron and the presence of Cr_2B resulted in an increase in the amount of trapped hydrogen in third peak for AHSS2. It is well known that dislocation is assigned to reversible trapping of hydrogen, whereas, austenite and precipitates are believed to irreversible trapping sites. It is evident from the obtained results that the irreversible-to-reversible trap ratio of AHSS2 is higher than that of AHSS1. Nonetheless, AHSS2 exhibited higher HE susceptibility than AHSS1. Needless to emphasis the role of precipitates as an irreversible trap in mitigating HE susceptibility [47]; However, crack initiation and propagation were clearly surrounding precipitates (Cr_2B and $Cr_{23}C_6$) in the presence of hydrogen, as shown in Figs. 8, 9. It can be concluded that the competitive effects of precipitates in the presence of hydrogen and the crucial role of precipitate type on the HE susceptibility need to be further investigated.

the fracture behavior induced by hydrogen is heavily influenced by the interplay between hydrogen and lattice defects, with particular emphasis on the interaction between dislocations and hydrogen [48–50]. The hydrogen charging significantly enhanced the dislocation density in both steels (Figs. 6, 7), similar result has been reported in the literature [51]. Dislocations were often anchored by precipitates and in some areas after hydrogen charging; they were grouped in tangles to create primitive cell structures [52]. Hydrogen accumulations are crucial to failure, and it is likely that the increase in dislocation density after hydrogen charging in the present study may be correlated to the increase in strain in the strain field surrounding precipitates, providing a local source of hydrogen [52]. Therefore, the difference in embrittlement between AHSS1 and AHSS2 seems reasonable.

The Taylor factor mappings offer an approximation of the yield response for each grain orientation ascertained by the EBSD scan concerning the applied stress state direction [53]. Grains with a decreased Taylor factor (indicated by the color blue) are deemed to possess appropriate orientations for slip, whereas grains with a higher Taylor factor (red color) are more challenging to deform plastically and may serve as initiation sites for cracks. Consequently, the development of cracks and undesired fractures are expected [54]. Figs. 11 and 12 show the Taylor factor maps of AHSS1 and AHSS2 samples following an interrupted tensile test. The hydrogen-charged samples were found to have a higher number of grains with a greater Taylor factor. The larger proportion of high Taylor factor grains produced in the hydrogen-charged specimen is highly susceptible to plastic instability, promoting fracture propagation. Similarly, several studies [55,56] have observed that grains with high Taylor factors are prone to crack propagation.

Fig. 13. displays the Taylor factor images acquired via EBSD from two locations where cracks occurred during tensile testing. The red region, which constitutes a significant portion, indicates the presence of intense plastic deformation and a high density of dislocations, leading to the formation of highly stressed grains that have a greater impact on fracture development. The Taylor factor exhibits a uniform distribution of damaged grains in both locations. Additionally, regions with a high Taylor factor correspond to areas with a significantly elevated stored energy in the specimens. While the plastic deformation resulting from the tensile test was influenced by the Taylor factor analysis, the areas that fractured exhibited more robust plastic behavior. The study's findings suggest that local high strain is prevalent near grain boundaries, particularly in the vicinity of fractures. It is important to highlight that greater misorientation is associated with a higher strain field. The Taylor factor was observed to be larger in the locations where cracks occurred (Fig. 13b, d), but many grains in non-cracked regions exhibited signs of being well-suited for slip deformation. In non-cracked areas, significant mismatches in Taylor factor values between neighboring grains were identified as potential sites for the susceptibility of intergranular cracking as a result of localized strain incompatibilities [57]. The findings of the study demonstrate that significant local strain fields raise either at or in proximity to grain boundaries as a result of dislocation accumulation during plastic deformation. Cracks were observed in both specimens near grains with high Taylor factor values, indicating fracture nucleation and propagation due to increased internal stress/energy caused by higher misorientation. The grains in the vicinity of the crack

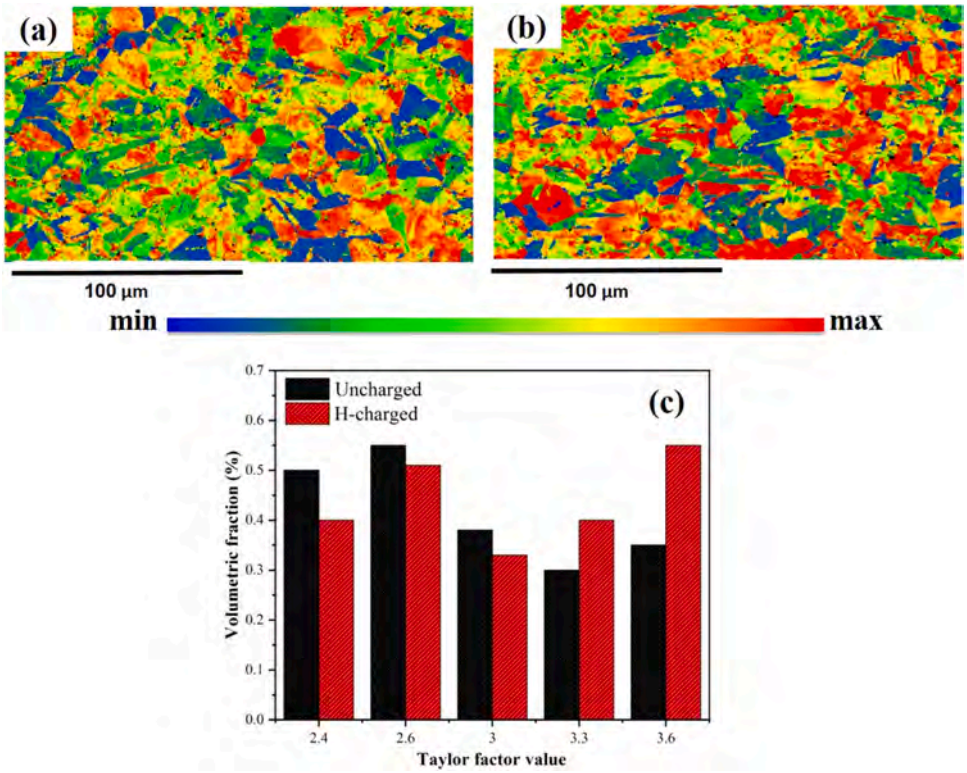

Fig. 11. Taylor factor maps of interrupted tensile test at strain of 83% for AHSS1, a) uncharged, b) H-charged, c) Taylor factor values.

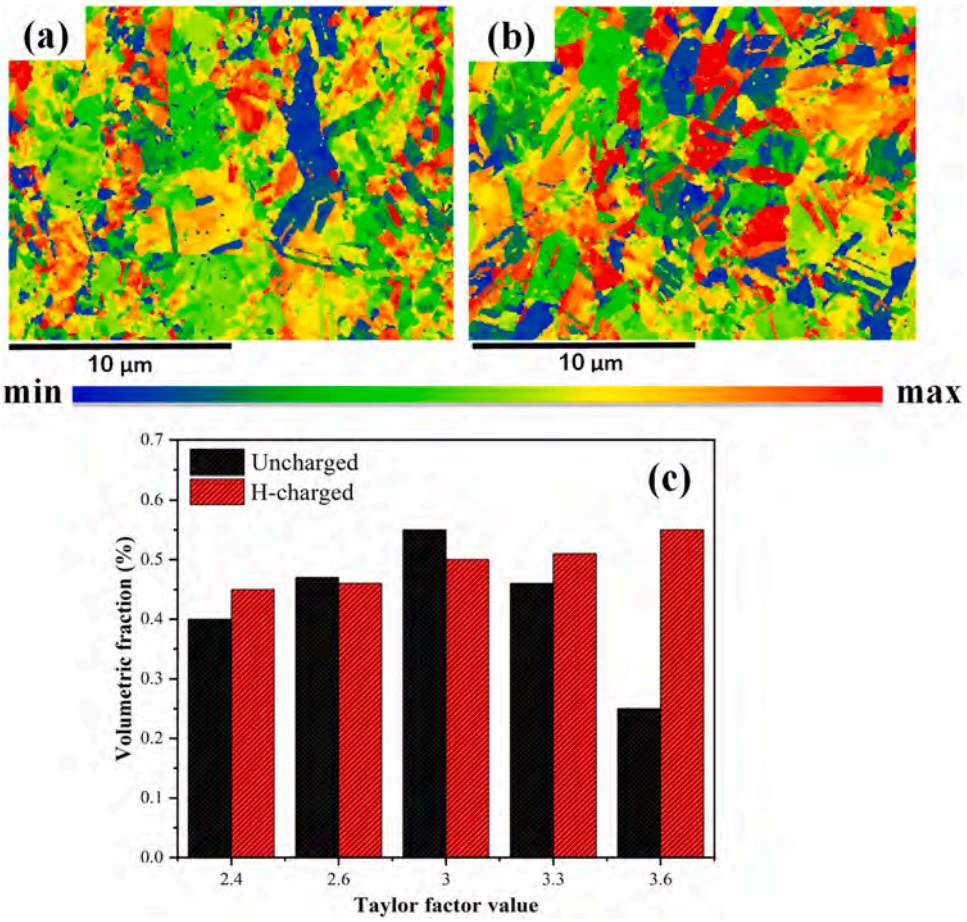

Fig. 12. Taylor factor maps of interrupted tensile test at strain of 6% for AHSS2, a) uncharged, b) H-charged, c) Taylor factor values.

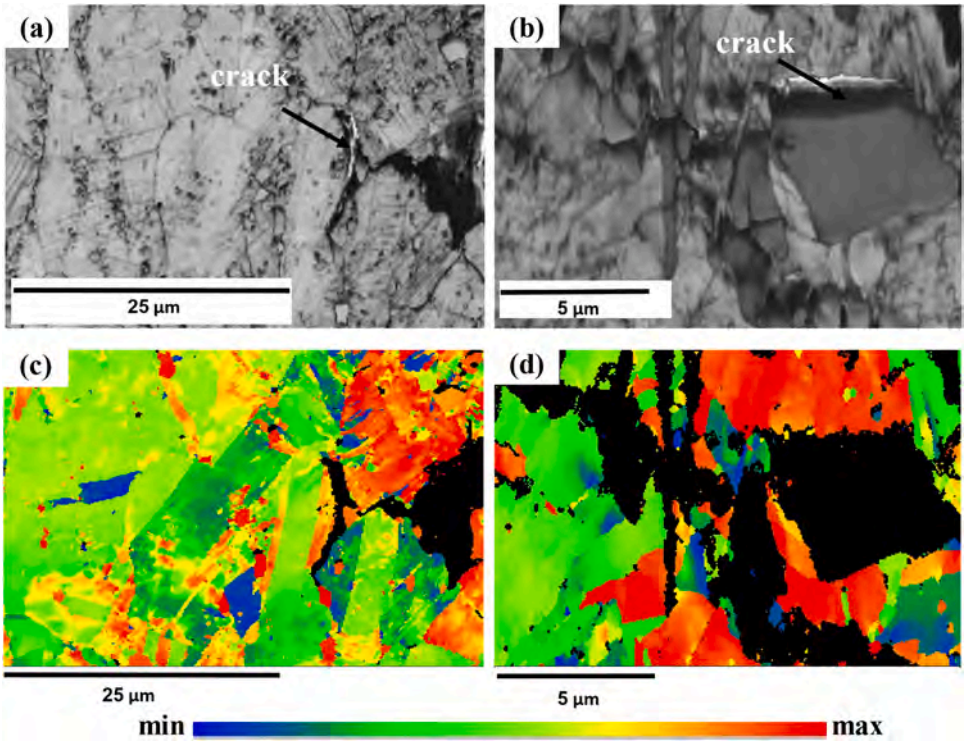

Fig. 13. SEM and distribution of Taylor factor maps in cracked areas after hydrogen charging: a, c) AHSS1, b, d) AHSS2.

paths in both regions had high Taylor factors, implying that energy was stored within the grains, and that additional straining resulted in increased plastic straining. Intergranular fracture occurs when a crack reaches a grain and spreads to the next high Taylor factor grain according to loading direction and crystal orientation [58]. Furthermore, fractures that propagated favorably along grains with high Taylor factor exhibited a reduced resistance to crack growth.

5. Conclusions

In the current study, the hydrogen embrittlement of FeCCrNiB0Si (AHSS1) and FeCCrNiB2Si (AHSS2) alloy systems has been evaluated through the mechanical properties, EBSD analysis, and TDS curves. The main conclusions are as follows:

1-Hydrogen charging deteriorated the mechanical properties of both steels. The hydrogen embrittlement index (I_{HE}) was 14 and 32 for AHSS1 and AHSS2, respectively. In addition, fracture toughness estimated by micro indentation reduced after hydrogen charging by 5% and 7.5% for AHSS1 and AHSS2, respectively.

2- Hydrogen charging resulted in a rise in the density of dislocations, thereby enhancing the local plasticity. In the other hand, the addition of boron in AHSS resulted in an increase in plastic strain incompatibility at the Cr_2B/γ interface, which cause interfaces decohesion and enhanced the propagation of crack.

3-The Taylor factor analysis showed the hydrogen charged specimens had higher volume fraction of grains with great Taylor factor value compared to uncharged samples. Furthermore, it was found that grains with a high amount of the Taylor factor were prone to the initiation and propagation of cracks when exposed to hydrogen.

4- TDS analysis showed the dislocation as a reversible trap while the austenite phase and precipitates were considered as an irreversible hydrogen trapping site. In addition, the ratio of irreversible to reversible traps was greater for AHSS2 than AHSS1.

Author Statement

We declare that this manuscript is original, has not been published before and is not currently being considered for publication elsewhere. We confirm that the manuscript has been read and approved by all named authors and that there are no other persons who satisfied the criteria for authorship but are not listed. We further confirm that the order of authors listed in the manuscript has been approved by all of us. We understand that the Corresponding Author is the sole contact for the Editorial process. He is responsible for communicating with the other authors about progress, submissions of revisions and final approval of proofs.

CRediT authorship contribution statement

Askari-Paykani Mohsen: Methodology, Project administration. **Vergani Laura Maria:** Methodology, Project administration. **Shahverdi Hamid Reza:** Methodology, Project administration. **Norouzi Ehsan:** Conceptualization, Data curation, Formal analysis, Investigation, Writing – original draft, Writing – review & editing. **Miresmaeili Reza:** Funding acquisition, Investigation, Resources, Supervision, Validation, Writing – review & editing.

Declaration of Competing Interest

The authors declare that they have no known competing financial interests or personal relationships that could have appeared to influence the work reported in this paper.

Data Availability

Data will be made available on request.

References

[1] S. Keeler, M. Kimchi, P.J. Mooney, Advanced high-strength steels application guidelines version 5.0, World Auto. Steel 276 (2014).
[2] H. Kaesche, Corrosion of Metals: Physicochemical Principles and Current Problems, Springer Science & Business Media, 2003.
[3] T. Depover, L. Duprez, K. Verbeken, E. Wallaert, M. Verhaege, In-situ mechanical evaluation of hydrogen embrittlement for TRIP, FB, DP and HSLA steels, Steel Hydrog. Confrerence (2011) 31–42.
[4] L. Moli-Sanchez, Z. Zermout, L. Duprez, L. Malet, Hydrogen embrittlement of 4 martensitic steels with strength levels above 1000 MPa Proc. 2nd Int Conf. Met. Hydrog., Ghent, Belg. 2014 70 84.
[5] S. Pallaspuro, H. Yu, A. Kisko, D. Porter, Z. Zhang, Fracture toughness of hydrogen charged as-quenched ultra-high-strength steels at low temperatures, Mater. Sci. Eng.: A 688 (2017) 190–201.
[6] J. Venezuela, Q. Zhou, Q. Liu, H. Li, M. Zhang, M.S. Dargusch, A. Atrens, The influence of microstructure on the hydrogen embrittlement susceptibility of martensitic advanced high strength steels, Mater. Today Commun. 17 (2018) 1–14.
[7] J. Venezuela, F.Y. Lim, L. Liu, S. James, Q. Zhou, R. Knibbe, M. Zhang, H. Li, F. Dong, M.S. Dargusch, Hydrogen embrittlement of an automotive 1700 MPa martensitic advanced high-strength steel, Corros. Sci. 171 (2020) 108726.
[8] M. Asadipoor, J. Kadkhodapour, A. Pourkamali Anaraki, S. Sharifi, A.C. Darabi, A. Barnoush, Experimental and numerical investigation of hydrogen embrittlement effect on microdamage evolution of advanced high-strength dual-phase steel, Met. Mater. Int. 27 (2021) 2276–2291.
[9] Q.S. Allen, T.W. Nelson, Microstructural evaluation of hydrogen embrittlement and successive recovery in advanced high strength steel, J. Mater. Process. Technol. 265 (2019) 12–19.
[10] A. Drexler, C. Bergmann, G. Manke, V. Kokotin, K. Mraczek, M. Pohl, W. Ecker, On the local evaluation of the hydrogen susceptibility of cold-formed and heat treated advanced high strength steel (AHSS) sheets, Mater. Sci. Eng.: A 800 (2021) 140276.
[11] M. Nagumo, Fundamentals of hydrogen embrittlement, Springer,, 2016.
[12] M.Y. Panchenko, G.G. Maier, I.A. Tumbusova, S.V. Astafurov, E.V. Melnikov, V. A. Moskvina, A.G. Burlachenko, Y.A. Mirovoy, Y.P. Mironov, N.K. Galchenko, The effect of age-hardening mechanism on hydrogen embrittlement in high-nitrogen steels, Int. J. Hydrog. Energy 44 (2019) 20529–20544.
[13] G. Álvarez, L. Peral, C. Rodríguez, T. García, F. Belzunce, Hydrogen embrittlement of structural steels: Effect of the displacement rate on the fracture toughness of high-pressure hydrogen pre-charged samples, Int. J. Hydrog. Energy 44 (2019) 15634–15643.
[14] M. Koyama, K. Ichii, K. Tsuzaki, Grain refinement effect on hydrogen embrittlement resistance of an equiatomic CoCrFeMnNi high-entropy alloy, Int. J. Hydrog. Energy 44 (2019) 17163–17167.
[15] M. Askari-Paykani, H.R. Shahverdi, R. Miresmaeili, Microstructural evolution and mechanical properties of a novel FeCrNiBSi advanced high-strength steel: Slow, accelerated and fast casting cooling rates, Mater. Sci. Eng.: A 668 (2016) 188–200.
[16] M. Askari-Paykani, H.R. Shahverdi, R. Miresmaeili, Effect of Boron Addition on Microstructural Evolution and Room-Temperature Mechanical Properties of Novel Fe 66− x CrNiB x Si (x= 0, 0.25, 0.50 and 0.75 wt Pct) Advanced High-Strength Steels, Metall. Mater. Trans. A 47 (2016) 5423–5437.
[17] M. Askari-Paykani, H.R. Shahverdi, R. Miresmaeili, First and third generations of advanced high-strength steels in a FeCrNiBSi system, J. Mater. Process. Technol. 238 (2016) 383–394.
[18] M. Askari-Paykani, H.R. Shahverdi, R. Miresmaeili, H. Beladi, Second-phase hardening and rule of mixture, microbands and dislocation hardening in Fe67. 4− xCr15. 5Ni14. 1Si3. 0Bx (x= 0, 2) alloy systems, Mater. Sci. Eng.: A 715 (2018) 214–225.
[19] H. Andersson, Analysis of a model for void growth and coalescence ahead of a moving crack tip, J. Mech. Phys. Solids 25 (1977) 217–233.
[20] J. Gong, H. Miao, Z. Peng, On the contact area for nanoindentation tests with Berkovich indenter: case study on soda-lime glass, Mater. Lett. 58 (2004) 1349–1353.
[21] M. He, F. Li, N. Ali, A normalized damage variable for ductile metals based on toughness performance, Mater. Sci. Eng.: A 528 (2011) 832–837.
[22] J. Lemaitre, J. Dufailly, Damage measurements, Eng. Fract. Mech. 28 (1987) 643–661.
[23] W.C. Oliver, G.M. Pharr, Measurement of hardness and elastic modulus by instrumented indentation: Advances in understanding and refinements to methodology, J. Mater. Res. 19 (2004) 3–20.
[24] G. Pharr, Measurement of mechanical properties by ultra-low load indentation, Mater. Sci. Eng.: A 253 (1998) 151–159.
[25] G. Sih, E. Chen, Dilatational and distortional behavior of cracks in magnetoelectroelastic materials, Theor. Appl. Fract. Mech. 40 (2003) 1–21.
[26] G. Sih, G. Sih, A three-dimensional strain energy density factor theory of crack propagation, Mech. Fract. Initiat. Propag.: Surf. Vol. Energy Density Appl. Fail. Criterion (1991) 23–56.
[27] C.Y. Tang, W. Tai, Material damage and forming limits of textured sheet metals, J. Mater. Process. Technol. 99 (2000) 135–140.
[28] S. Zügner, K. Marquardt, I. Zimmermann, Influence of nanomechanical crystal properties on the comminution process of particulate solids in spiral jet mills, Eur. J. Pharm. Biopharm. 62 (2006) 194–201.
[29] X. Zhu, W. Li, H. Zhao, L. Wang, X. Jin, Hydrogen trapping sites and hydrogen-induced cracking in high strength quenching & partitioning (Q&P) treated steel, Int. J. Hydrog. Energy 39 (2014) 13031–13040.

[30] Z. Yan, D. Wang, X. He, W. Wang, H. Zhang, P. Dong, C. Li, Y. Li, J. Zhou, Z. Liu, Deformation behaviors and cyclic strength assessment of AZ31B magnesium alloy based on steady ratcheting effect, Mater. Sci. Eng.: A 723 (2018) 212–220.
[31] M. Dadfarnia, A. Nagao, S. Wang, M.L. Martin, B.P. Somerday, P. Sofronis, Recent advances on hydrogen embrittlement of structural materials, Int. J. Fract. 196 (2015) 223–243.
[32] R. Petrov, L. Kestens, A. Wasilkowska, Y. Houbaert, Microstructure and texture of a lightly deformed TRIP-assisted steel characterized by means of the EBSD technique, Mater. Sci. Eng.: A 447 (2007) 285–297.
[33] S.H. Zaferani, R. Miresmaeili, M.K. Pourcharmi, Mechanistic models for environmentally-assisted cracking in sour service, Eng. Fail. Anal. 79 (2017) 672–703.
[34] M. Koyama, C.C. Tasan, E. Akiyama, K. Tsuzaki, D. Raabe, Hydrogen-assisted decohesion and localized plasticity in dual-phase steel, Acta Mater. 70 (2014) 174–187.
[35] M. Ranjbar, R. Miresmaeili, M.R. Naimi-Jamal, M. Mirzaei, Effect of microstructure on the mechanical properties and fracture toughness of API X65 pipeline steel in the presence of hydrogen, Met. Mater. Int. 27 (2021) 3918–3934.
[36] T.S. Byun, J.W. Kim, J.H. Hong, A theoretical model for determination of fracture toughness of reactor pressure vessel steels in the transition region from automated ball indentation test, J. Nucl. Mater. 252 (1998) 187–194.
[37] J.-S. Lee, J.-i Jang, B.-W. Lee, Y. Choi, S.G. Lee, D. Kwon, An instrumented indentation technique for estimating fracture toughness of ductile materials: A critical indentation energy model based on continuum damage mechanics, Acta Mater. 54 (2006) 1101–1109.
[38] R. Matsumoto, S. Taketomi, S. Matsumoto, N. Miyazaki, Atomistic simulations of hydrogen embrittlement, Int. J. Hydrog. Energy 34 (2009) 9576–9584.
[39] Y. Wang, X. Wu, X. Li, W. Wu, J. Gong, Combined effects of prior plastic deformation and sensitization on hydrogen embrittlement of 304 austenitic stainless steel, Int. J. Hydrog. Energy 44 (2019) 7014–7031.
[40] Q. Song, Z. Li, Y. Zhu, M. Huang, On the interaction of solute atoms with circular inhomogeneity and edge dislocation, Int. J. Plast. 111 (2018) 266–287.
[41] L. Mao, Z. Luo, C. Huang, H. Zhou, X. Zhang, Exploring the hydrogen embrittlement behavior in nickel-economized austenitic stainless steel: Investigating the role of manganese in modifying hydrogen-induced crack mechanisms, Corros. Sci. 226 (2024) 111691.
[42] H. Cheng, H. Luo, Z. Pan, X. Wang, Q. Zhao, X. Li, Hydrogen embrittlement of a precipitation-strengthened high-entropy alloy, Corros. Sci. 227 (2024) 111708.
[43] M. Martin, B. Somerday, R. Ritchie, P. Sofronis, I. Robertson, Hydrogen-induced intergranular failure in nickel revisited, Acta Mater. 60 (2012) 2739–2745.
[44] L. Cho, P.E. Bradley, D.S. Lauria, M.L. Martin, M.J. Connolly, J. Benzing, E.J. Seo, K.O. Findley, J.G. Speer, A.J. Slifka, Characteristics and mechanisms of hydrogen-induced quasi-cleavage fracture of lath martensitic steel, Acta Mater. 206 (2021) 116635.
[45] P. Ma, L. Qian, J. Meng, S. Liu, F. Zhang, Fatigue crack growth behavior of a coarse-and a fine-grained high manganese austenitic twin-induced plasticity steel, Mater. Sci. Eng.: A 605 (2014) 160–166.
[46] E. Norouzi, R. Miresmaeili, H.R. Shahverdi, M. Askari-Paykani, L.M. Vergani, Hydrogen embrittlement behavior in FeCCrNiBSi TRIP steel, J. Mater. Res. Technol. 23 (2023) 859–868.
[47] T. Depover, K. Verbeken, Hydrogen trapping and hydrogen induced mechanical degradation in lab cast Fe-C-Cr alloys, Mater. Sci. Eng.: A 669 (2016) 134–149.
[48] G. Hachet, A. Oudriss, A. Barnoush, R. Milet, D. Wan, A. Metsue, X. Feaugas, The influence of hydrogen on cyclic plasticity of< 001> oriented nickel single crystal. Part I: Dislocation organisations and internal stresses, Int. J. Plast. 126 (2020) 102611.
[49] G.M. Castelluccio, C.B. Geller, D.L. McDowell, A rationale for modeling hydrogen effects on plastic deformation across scales in FCC metals, Int. J. Plast. 111 (2018) 72–84.
[50] L. Wan, W.T. Geng, A. Ishii, J.-P. Du, Q. Mei, N. Ishikawa, H. Kimizuka, S. Ogata, Hydrogen embrittlement controlled by reaction of dislocation with grain boundary in alpha-iron, Int. J. Plast. 112 (2019) 206–219.
[51] E. Norouzi, R. Miresmaeili, H.R. Shahverdi, M. Askari-Paykani, L.M. Vergani, Effect of hydrogen on the deformation mechanisms of metastable 304 austenitic stainless steel, Mater. Lett. 338 (2023) 134021.
[52] P. Gong, A. Turk, J. Nutter, F. Yu, B. Wynne, P. Rivera-Diaz-del-Castillo, W. M. Rainforth, Hydrogen embrittlement mechanisms in advanced high strength steel, Acta Mater. 223 (2022) 117488.
[53] U. Kocks, H. Mecking, Physics and phenomenology of strain hardening: the FCC case, Prog. Mater. Sci. 48 (2003) 171–273.
[54] A.S. Azar, L.-E. Svensson, B. Nyhus, Effect of crystal orientation and texture on fatigue crack evolution in high strength steel welds, Int. J. Fatigue 77 (2015) 95–104.
[55] M. Masoumi, C.C. Silva, M. Béreš, D.H. Ladino, H.F.G. de Abreu, Role of crystallographic texture on the improvement of hydrogen-induced crack resistance in API 5L X70 pipeline steel, Int. J. Hydrog. Energy 42 (2017) 1318–1326.
[56] M. Masoumi, C.C. Silva, H.F.G. de Abreu, Effect of crystallographic orientations on the hydrogen-induced cracking resistance improvement of API 5L X70 pipeline steel under various thermomechanical processing, Corros. Sci. 111 (2016) 121–131.
[57] M. Liu, C. Yang, G. Cao, A.M. Russell, Y. Liu, X. Dong, Z. Zhang, Effect of microstructure and crystallography on sulfide stress cracking in API-5CT-C110 casing steel, Mater. Sci. Eng.: A 671 (2016) 244–253.
[58] W. Zhao, R. Xin, Z. He, Y. Wang, Contribution of anodic dissolution to the corrosion fatigue crack propagation of X80 steel in 3.5 wt% NaCl solution, Corros. Sci. 63 (2012) 387–392.